Research Article

Wenzhao Wang#, Boqing Zhang#, Lihong Zhao#, Mingxin Li, Yanlong Han, Li Wang, Zhengdong Zhang, Jun Li, Changchun Zhou*, and Lei Liu*

Fabrication and properties of PLA/nano-HA composite scaffolds with balanced mechanical properties and biological functions for bone tissue engineering application

https://doi.org/10.1515/ntrev-2021-0083
received July 23, 2021; accepted September 1, 2021

Abstract: Repair of critical bone defects is a challenge in the orthopedic clinic. 3D printing is an advanced personalized manufacturing technology that can accurately shape internal structures and external contours. In this study, the composite scaffolds of polylactic acid (PLA) and nano-hydroxyapatite (n-HA) were manufactured by the fused deposition modeling (FDM) technique. Equal mass PLA and n-HA were uniformly mixed to simulate the organic and inorganic phases of natural bone. The suitability of the composite scaffolds was evaluated by material characterization, mechanical property, and *in vitro* biocompatibility, and the osteogenesis induction *in vitro* was further tested. Finally, the printed scaffold was implanted into the rabbit femoral defect model to evaluate the osteogenic ability *in vivo*. The results showed that the composite scaffold had sufficient mechanical strength, appropriate pore size, and biocompatibility. Most importantly, the osteogenic induction performance of the composite scaffold was significantly better than that of the pure PLA scaffold. In conclusion, the PLA/n-HA scaffold is a promising composite biomaterial for bone defect repair and has excellent clinical transformation potential.

Keywords: 3D printing, polylactic acid, nano-hydroxyapatite, bone defect, composited biomaterials

1 Introduction

Critical bone defects cannot heal themselves, and the current autogenous bone grafting is not ideal for repairing critical defects [1]. Revision surgeries are usually required to repair bone defects clinically [2,3]. In addition, the autologous bone source is less, and postoperative complications are more [4]. For a long time, researchers have been working to develop an alternative to artificial bone grafts, known as synthetic bone graft substitutes [1]. The primary artificial scaffold was simply to fill the defect area, but with the progress of technology, the current expectation of synthetic bone defect scaffold has become active induction of bone regeneration and reconstruction of the primary bone [5]. The exploration of scaffolds in bone tissue engineering is divided into two aspects: one is to explore and configure the scaffolds that can support and

# These authors contributed equally to this work.

*** Corresponding author: Changchun Zhou,** National Engineering Research Center for Biomaterials, Sichuan University, Chengdu 610064, China; College of Biomedical Engineering, Sichuan University, Chengdu 610064, China, e-mail: changchunzhou@scu.edu.cn
*** Corresponding author: Lei Liu,** Orthopedic Research Institute, Department of Orthopedics, National Clinical Research Center for Geriatrics, West China Hospital, Sichuan University, Chengdu 610041, China, e-mail: liuinsistence@163.com
Wenzhao Wang, Lihong Zhao, Mingxin Li, Jun Li: Orthopedic Research Institute, Department of Orthopedics, National Clinical Research Center for Geriatrics, West China Hospital, Sichuan University, Chengdu 610041, China
Boqing Zhang: National Engineering Research Center for Biomaterials, Sichuan University, Chengdu 610064, China; College of Biomedical Engineering, Sichuan University, Chengdu 610064, China
Yanlong Han, Li Wang: Department of Orthopedics, The People's Hospital of Xinjiang Uygur Autonomous Region, Urumqi 830001, China
Zhengdong Zhang: Orthopedic Research Institute, Department of Orthopedics, National Clinical Research Center for Geriatrics, West China Hospital, Sichuan University, Chengdu 610041, China; Department of Orthopedics, The First Affiliated Hospital of Chengdu Medical College, Chengdu, Sichuan, China

induce bone tissue growth, that is, to manufacture a porous structure scaffold to fill bone defects [6]. The pore structure is also the continuous inward growth and material exchange channels of bone tissue [7]. Liquid can be nourished and transported through the pores; migrated stem cells, bone cells, macrophages, and other cells can cross grow through the pores [8]. Regenerated blood vessels and bone tissue can survive and develop in these pores [9,10]; the other is to find and develop manufacturing methods to improve biofunctions [6,11].

Currently, porous bone scaffolds can be manufactured by a variety of methods. Traditional methods include phase separating, particle leaching, gas foaming, or freeze-drying, which cannot control the pore size, shape, and interconnection [12]. However, these techniques do not produce the precise structure of a 3D scaffold [13]. 3D printing shows great material fabrication ability, which bridges the divergence between artificially engineered tissue structures and natural tissues [9]. 3D printing can print the scaffold layer by layer according to the specific computer-aided design modeling [14]. 3D artificial bone tissue can be easily created using biological ink, which exists in the form of a viscous fluid. Different parameters are considered to develop specific bio-inks, such as printability, mechanical integrity, and so on. [15]. Among various 3D printing technologies, fused deposition modeling (FDM) 3D printing technology is portable, simple, accurate, and has great potential for clinical use [16,17].

The polymer material has sufficient mechanical properties and is suitable for the repair of critical bone defects [16,18]. Notably, osteogenic differentiation can be facilitated by polymer scaffolds [19]. Polycaprolactone, polyglycolic acid, and polylactic acid (PLA), as well as their copolymers, are widespread synthetic biomaterials characterized by their biodegradability [20,21]. Among them, poly-lactic acid (PLA) has been defined as a biomaterial with potential clinical applications in many studies due to its slow degradation properties and reliable biocompatibility [22,23]. However, the drawback of pure polymer scaffolds is the lack of osteogenic inducement, which is also the main reason why researchers were chosen to explore composite materials [24]. Hydroxyapatite (HA) is a natural mineral form of calcium phosphate, which is the main mineral component of vertebrate bones and teeth [25]. HA has excellent biocompatibility and biological activity [9]. The proliferation of osteoblasts and the formation of chemical bonds with the natural bone were promoted by HA in the process of bone formation [26–28]. Compared with the HA, nano-HA [n-HA] overcomes the shortcomings of traditional HA, such as high brittleness [29,30]. In addition, n-HA has better dispersibility to attach to the cell membrane and more suitable as a filler or a coating material [31,32].

In this study, n-HA and PLA with the same mass were fabricated into composite scaffolds. The characterization, mechanical properties, *in vitro* biocompatibility, and osteogenic inducibility of the composite scaffold were systematically examined, and further *in vivo* experiments were conducted in a rabbit femoral defect model for 3 months. The results show that the PLA/n-HA composite scaffolds have good biocompatibility and osteogenic induction ability by simulating organic and inorganic materials in bone tissue, simulating the natural bone matrix environment, and having the potential of clinical transformation in the repair of critical bone defects.

2 Materials and methods

2.1 Preparation of composite materials and printing of scaffolds

n-HA powders with an average diameter of 75 ± 20 nm (NERCB, Chengdu, China) were dissolved in acetone by magnetic stirring for 48 h, while PLA (Daigang Biomaterial, Jinan, China) with an average molecular weight of 200,000 was dissolved in dichloromethane. Then, the two solutions were mixed and stirred under ultrasonic for 2 h to obtain the compound solution. The composite solution was volatilized for a week at room temperature (24–26°C) in the fume hood and then put into a vacuum drying oven with the temperature set at 50°C. After vacuum drying for 48 h, the PLA/n-HA composite material was obtained. The dry composite material was put into the high-speed crusher, and the grinding stopped after the sample was completely crushed into powder. The temperature of the material bin of the drawing machine was set at 160°C, and the temperature of the extruder was set at 165°C. The composite material powder was poured into the material bin, the filament with a diameter of 1.75 ± 0.05 mm was extruded, and the extruded filament material was collected. The 3D model was built using SolidWorks software (Dassault Systems, France), and then the print path was planned using Simplify 3D (Cincinnati, USA). The thickness of each layer was 0.2 mm, and the printing speed was 60 mm/s. Finally, after applying the washable printing glue on the FDM printer platform, the composite filament material was put into the FDM printer to obtain the 3D printing

scaffold. The ratio used in the composite material group in this study was 5:5 mass ratio of PLA to n-HA. The control group was pure PLA.

2.2 Characterization and observation of scaffolds

The morphology of the composite material, filament, and 3D printed cell scaffold under natural light was recorded using a Leica (Germany) camera. The transmission electron microscope (TEM; Tecnai G2 F20 S-TWIN, FEI, USA) and atomic force microscope (AFM; SPA400, NSK Ltd, Japan) were used to observe n-HA particles. Scanning electron microscopy (SEM; JSE-5900LV, Japan) was used to evaluate the morphology of the gold sputter-coated particles, filaments, and the 3D-printed scaffolds. Energy-dispersive X-ray spectroscopy (EDS) detection was used to analyze the distribution in the material by Phenom ProX-SE (Netherlands). The 3D-printed blocks and cylinders were scanned by micro-computerized tomography (CT; Quantum GX, San Diego, USA) and reconstructed in three dimensions. The mechanical properties of the printed support were tested by an electronic universal testing machine (INSTRON, USA). The standard cylinder (Φ 6.5 mm × 13 mm) was stressed at a speed of 1 mm/min. The maximum compression stress described in this study referred to the compression stress when the specimen breaks (brittle material) or yields (elastic material) during the compression test.

2.3 Cell culture and biocompatibility test

Rabbit bone marrow mesenchymal stem cells (BMSCs) were cultured at 37°C in a humidified atmosphere of 5% CO_2. When the cells were passed to the fourth generation, they were seeded on a printed scaffold. Cell Counting Kit-8 (SolarBio, Beijing, China) was used to detect the influence of scaffolds on cell activity. To detect the effect of scaffold on cell activity, CCK8 experiment in this study was divided into three groups: negative control (NC) group without scaffold, PLA scaffold group, and composite material group. CCK8 solution of 10 µL was added to each well of a 96-well plate and incubated at 37°C for 2 h. The absorbance was measured at 450 nm using a microplate analyzer (Thermo Scientific, MA, USA). The cell-laden scaffolds dehydrated by gradient (70, 80, 90, and 100%) alcohol were observed under an electron microscope (JSE-5900LV). On the 1st, 4th, and 7th day, the cells were measured by the Live/Dead Cell Staining Kit (Abbkine, Wuhan, China) and photographed with a laser confocal microscope (Carl Zeiss, Germany). On the 1st, 4th, and 7th day, the cells were permeabilized with 0.1% Triton X-100 in PBS for 10 min, then F-actin staining reagent was added (Abbkine) after 30 min, and cells were photographed with a laser confocal microscope (Carl Zeiss).

2.4 Osteogenesis induction test

BMSCs were cultured in an osteogenesis induction medium for 7 days. The formulation of osteogenic induction medium was DMEM medium with 10% FBS, 10 mmol/L β-sodium glycerophosphate, 0.05 mmol/L vitamin C, 100 mmol/L dexamethasone, and 100 IU/mL penicillin–streptomycin. The alkaline phosphatase (ALP) activity was evaluated with the ALP Assay Kit (Beyotime, Shanghai, China). The cells were fixed with 4% paraformaldehyde solution, Alizarin Red S Staining reagent (Beyotime) was added for 30 min at room temperature, and cells were washed with distilled water. Images of ALP and Alizarin Red S stained scaffolds were acquired with a stereoscopic microscope (Carl Zeiss). BMSCs induced by osteogenesis for 7 days were used to collect total RNA. Total RNA was extracted from cultured BMSCs using the RNA extraction reagent (Servicebio, Wuhan, China). After the concentration and purity of RNA were tested with a spectrophotometer (Nanodrop 2000, Thermo Scientific, MA, USA), reverse transcription (RT) was performed. A 20-µL reaction system RT kit (Servicebio) was used for reverse transcription, and the reaction procedure was as follows: 25°C; 5 min, 42°C; 30 min, and 85°C; 5 s. qRT-PCR was performed using SYBR Green PCR kit (Servicebio) on an Applied Biosystems System. The PCR amplification procedure consisted of 95°C for 10 min, 40 cycles of 95°C for 15 s and 60°C for 30 s, and finally from 65 to 95°C. The signal was collected once for each temperature rise of 0.5°C. The study was performed in triplicate. The primer sequences were as follows:

OPN: **F**-GGCTAAACCCTGACCCATCTC, **R**-ATGGCTTTC AATGGACTTACTCG; *Runx2* **F**-CCAGAAGGCACAGACAGA AGC, **R**-ATGAGGAATGCGCCCTAAATC; *COL1a1* **F**-TGGT GAATCTGGACGTGAGGG, **R**-TTATGCCTCTGTCGCCCTGTT; *BMP2* **F**-ACCATGGGTTTGTGGTGGAA, **R**-CCGCTGTTTGTG TTTCGCTT; *GAPDH* **F**-TGAAGGTCGGAGTGAACGGAT, **R**-CGTTCTCAGCCTTGACCGTG.

2.5 *In vivo* experiment

New Zealand white rabbits (2–3 kg, male) were obtained from the Dossy Experimental Animals (Chengdu, China). All the experiments were approved by the Ethics Committee of Sichuan University. The rabbits were anesthetized with pentobarbital (40 mg/kg) injection and cut layer by layer to expose the femoral shaft. A trephine (Tiantian Dental Equipment, Changsha, China) with an inner diameter of 5 mm was used to drill the femoral shaft, and a 3D printed scaffold was implanted. After suturing, the rabbits were placed on a heating mat and returned to the cage after resuscitation. Femur samples were taken at 1 month, 2 months, and 3 months after surgery and fixed in 4% paraformaldehyde solution. 3D data were collected by micro-CT (Quantum GX, USA). The fixed samples were dehydrated with gradient (70, 80, 90, and 100%) ethyl alcohol and then embedding with resin. The embedded tissue was sliced into 5 µm tissue sections and stained with hematoxylin and eosin (HE).

2.6 Statistical analysis

Statistical analysis was conducted using GraphPad Prism Software (GraphPad Software Inc, USA), and data were expressed as mean ± standard deviation (SD). Statistical significance between the two groups was assessed using independent-samples *t*-test, while analysis of variance (ANOVA) with *post hoc* Dunnett's corrections was performed for comparison between two or more groups. $p < 0.05$ was considered statistically significant.

3 Results

3.1 Characterization of PLA/n-HA composite and scaffolds

After drying, the n-HA suspension was observed under SEM. The dried n-HA particles were aggregated into clusters (Figure 1a and b). Further observation by TEM showed that the diameter of n-HA particles was 50 and 80 nm (Figure 1c). The PLA/n-HA complex solution was dried at room temperature to obtain the composite blocks (Figure 2a), and then, the composite blocks were crushed into powder and processed into the filament (Figure 2b). The filament was a uniform white cylinder with a diameter of 1.75 mm (Figure 2c and d). The filament was processed into porous scaffolds with a diameter of 9 mm for *in vitro* experiment (Figure 2e) and cylinder for mechanical testing by an FDM 3D printer (Figure 2f). The forward, diagonal, and honeycomb printed cubes were CT scanned to test the printability of the composite filament. CT scan showed that the printed block had complete structure, regular shape, and clear pore structure (Figure 2g). EDS was used to detect the composition and element distribution in the rectangular area marked on the surface of the composite material. Carbon (C), phosphorus (P), calcium (Ca), and oxygen (O) were detected, demonstrating that no other components were mixed into the composite and no residual dichloromethane used in the processing was present (Figure 3a and b). The homogeneous distribution of n-HA in the composite material was confirmed by the uniform distribution of each element in the selected region (Figure 3c–f). Furthermore,

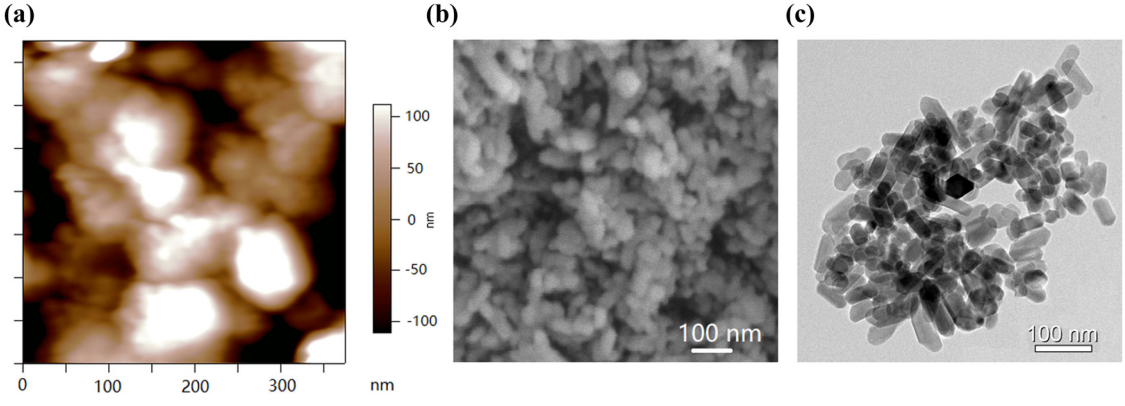

Figure 1: The morphology of the n-HA powders, based on the calculation of image J processing software, the average diameter of the HA powders was 75 ± 20 nm. (a) AFM image of the n-HA powders; (b) SEM image of the n-HA powders; and (c) TEM image of n-HA powders.

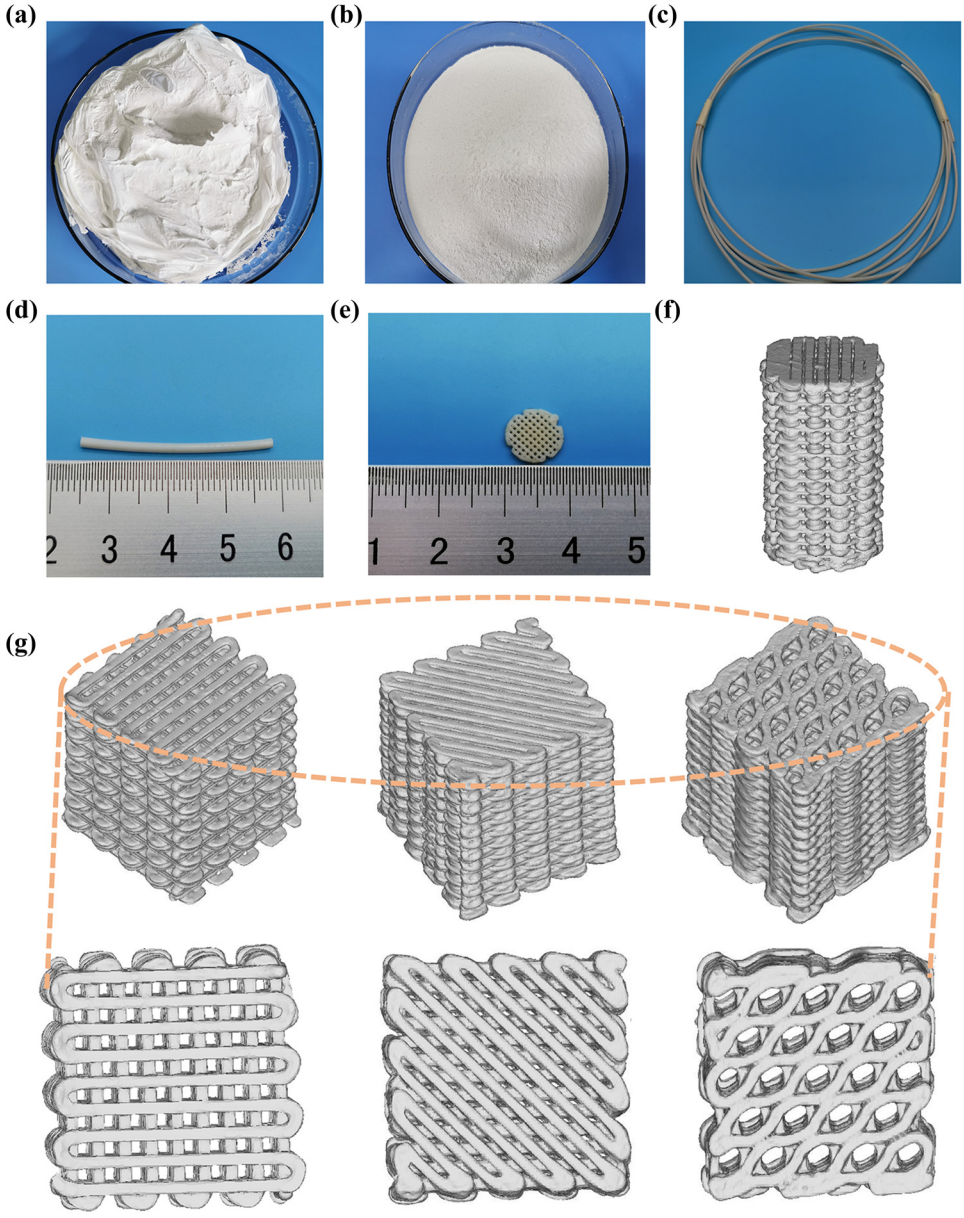

Figure 2: Manufacture of PLA/n-HA composites. (a) Dry raw PLA/n-HA material; (b) crushed raw PLA/n-HA materials; (c and d) PLA/n-HA composite filament; (e) 3D-printed PLA/n-HA composite cell scaffolds; (f) CT reconstruction of a 3D-printed composite cylinder; and (g) CT reconstruction of a 3D-printed (forward, diagonal, honeycomb) blocks.

SEM was used to observe the composite filament and scaffold. The surface and cross section of the filament materials in the PLA group was smooth, while the surface of the PLA + 50% n-HA group was rough (Figure 4a–d). The surface of the scaffold was similar to that of the filament. The PLA group was still smooth, while the surface of the PLA + 50% n-HA group was obviously uneven. When the surface of the scaffold was magnified 5,000 times, evenly distributed n-HA particles on the surface of the PLA + 50% n-HA group particles were clearly visible (Figure 4e and f). Subsequently, mechanical tests were conducted on the two groups of printed scaffolds. The PLA group was elastic material, and no cracking occurred after compression. However, the PLA + 50% n-HA group was brittle material, and the scaffold ruptured after compression (Figure 5a and b). After the addition of n-HA, the compressive strength of the composite scaffold decreased from 35.41 to 17.80 MPa.

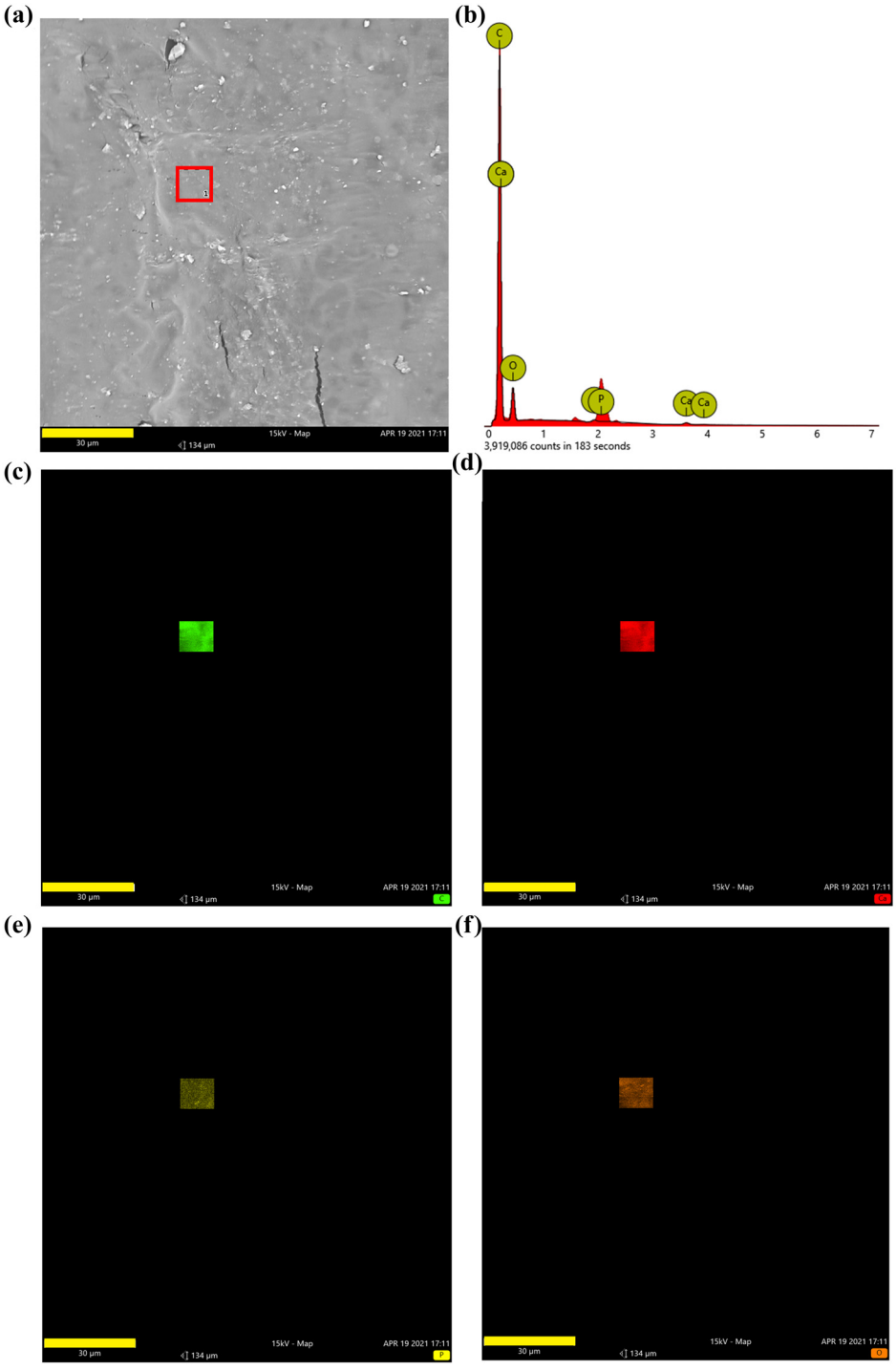

Figure 3: Composition of composite material. (a) EDS was used to detect the composition and element distribution in the rectangular area (marked in red) on the surface of the composite material; (b) carbon (C), calcium (Ca), phosphorus (P), and oxygen (O) were detected in the composite material; and (c–f) the distribution of C, Ca, P, and O (bar = 30 µm).

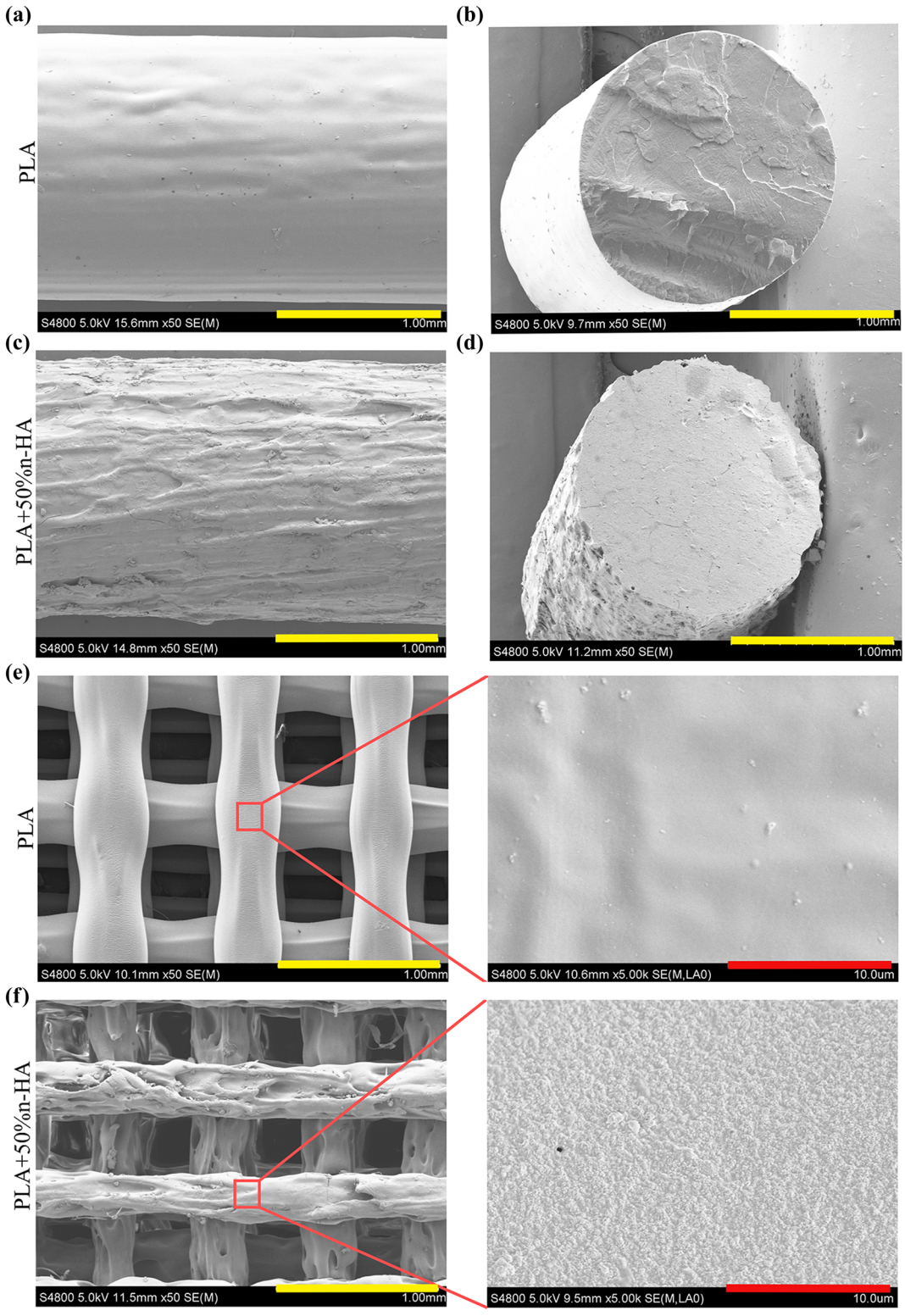

Figure 4: Filaments and 3D printed scaffolds under SEM. SEM images of the surface (a) and the cross section (b) of PLA filament; SEM images of the surface (c) and the cross section (d) of PLA/n-HA composite filament; (e) SEM image of 3D printed PLA scaffolds and its magnification image (right); and (f) SEM image of 3D printed PLA/n-HA composite scaffolds and its magnification image (right) (bars, yellow = 1 mm; red = 10 μm).

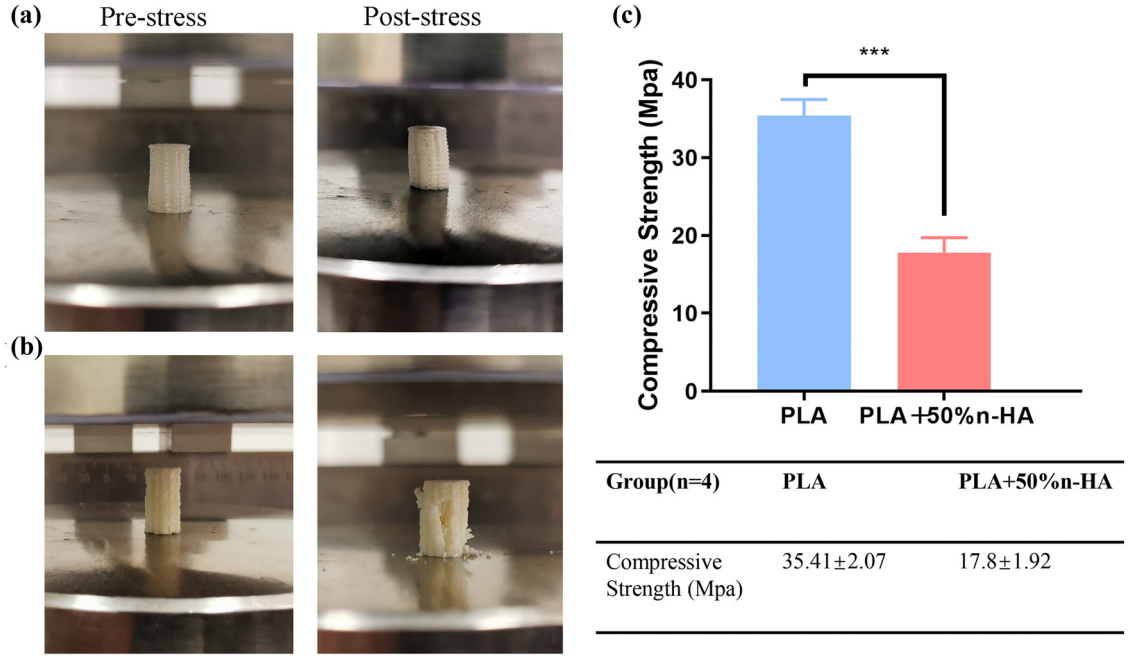

Group(n=4)	PLA	PLA+50%n-HA
Compressive Strength (Mpa)	35.41±2.07	17.8±1.92

Figure 5: Mechanical test of 3D-printed samples. (a) 3D-printed PLA cylinder before pressure test and after pressure test; (b) 3D-printed PLA/n-HA cylinder before pressure test and after pressure test; and (c) pressure test results. ***$p < 0.001$.

3.2 Biocompatibility of 3D-printed PLA/n-HA scaffolds

In vitro scaffolds incubated with BMSCs were used to test the biocompatibility of the composites. SEM images showed that the cells in both the PLA and PLA + 50% n-HA groups could grow and pave on the scaffold, the cells were well attached, and the pseudopod could be seen sticking out (Figure 6a). Cell activity and toxicity tests were performed on days 1, 4, and 7. The results revealed no significant differences among the NC, PLA, and PLA + 50% n-HA groups on days 1, 4, and 7, but significant differences were found between the time points (Figure 6b). Living dead dyeing and F-actin staining were stained on the 1, 4, and 7th day. It can be seen that within 7 days, the cells gradually proliferated on the scaffold and the cell gaps were gradually filled. The 3D image shows that the cells gradually overlap with the outline of the scaffold in three dimensions (Figure 6c). No dead cells stained red was found in the live staining, which proved that the scaffold had good biocompatibility. The complete absence of red dead cells in live death staining might be due to the fact that a small number of dead cells had been eluted during the PBS washing process. F-actin staining clearly indicated the spreading state of the BMSCs with red staining of the cytoskeleton and blue staining of the nucleus. Sporadic dispersal of cells was observed on the first day, and the cells were small and not fully spread out (Figure 6d). On day 4, the cells were more numerous and spread out, and the intercellular space became smaller. By day 7, the cells had grown and were pushing against each other. In addition, the growth state of cells along the outline of the scaffold was clearly shown in the 3D images.

3.3 *In vitro* osteogenic induction of the 3D-printed PLA/n-HA scaffolds

Alizarin Red S Staining identified calcium nodules formation of BMSCs on the composite scaffold and pure PLA scaffold. Calcium nodules stained red were sporadically distributed in the PLA scaffold group, while the number of calcium nodules in the composite group was significantly more than that in the PLA group (Figure 7a and b). ALP staining was performed to determine an early stage osteogenic differentiation of BMSCs on the composite scaffold and pure PLA scaffold. Stains in the composite scaffold group were darker and showed more color areas than those in the PLA group (Figure 7c and d). To investigate the osteogenic differentiation of BMSCs on pure PLA and composite scaffold, the expressions of Runt-related transcription factor 2 (*Runx2*), type I collagen a1 (*Col1a1*), osteopontin (*OPN*), and bone morphogenetic protein-2 (*BMP2*) were examined. PCR results showed

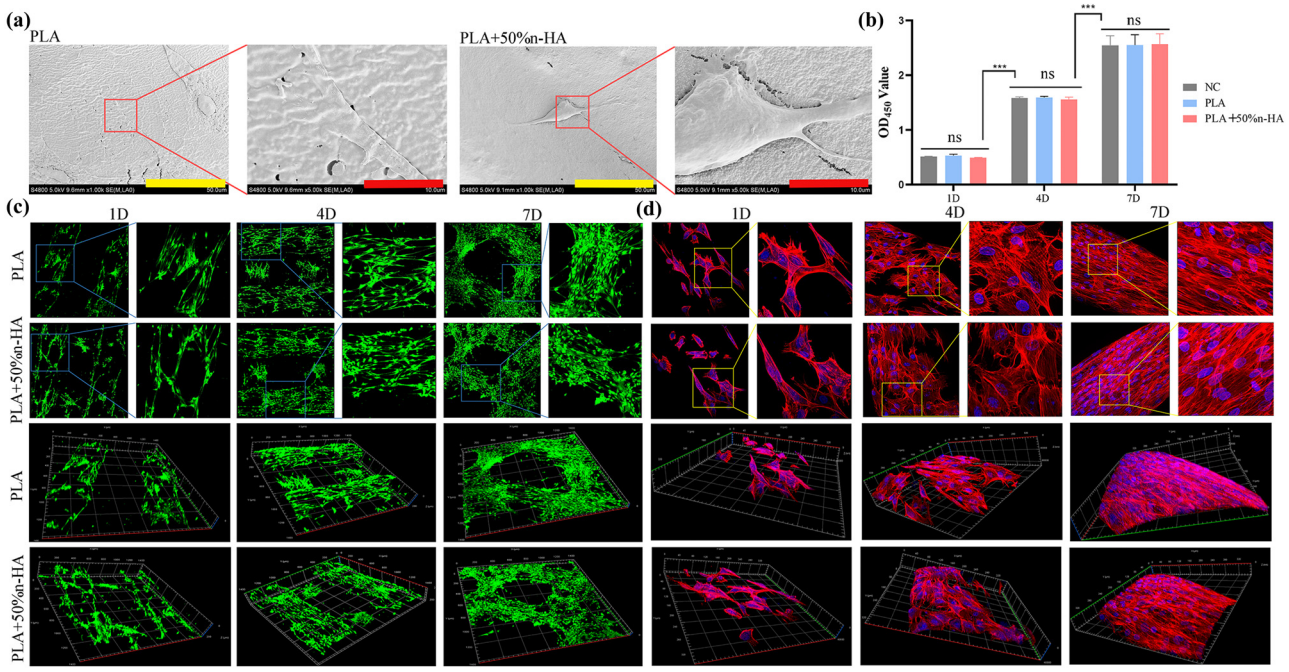

Figure 6: Biocompatibility of 3D-printed scaffolds. (a) 3D printing PLA and PLA/n-HA scaffolds loaded with BMSCs under SEM (bar, low power = 50 μm; high power = 10 μm); (b) cell activity and cytotoxicity tests of BMSCs on PLA and PLA/n-HA scaffolds for 1, 4, and 7 days; (c) live/dead cell staining of BMSCs on 3D printing PLA and PLA/n-HA scaffolds for 1, 4, and 7 days; and (d) cytoskeleton F-actin-stained BMSCs on scaffolds on day 1, 4, and 7. ***$p < 0.001$.

that the expression levels of the four osteogenic related genes in the composite material group were significantly higher than that in the PLA group (Figure 7e–h).

3.4 *In vivo* osteogenic induction of 3D-printed PLA/n-HA scaffolds

A rabbit model of the femoral defect was used to test the osteogenic ability of the scaffold *in vivo* (Figure S1). Rabbit femur and inserted PLA or composite scaffold were stained with HE at 1, 2, and 3 months after implantation. HE staining showed that the 3D-printed scaffold after implantation could be well embedded into the bone defect site, indicating that the scaffold had a good ability of osteointegration. No inflammatory cell aggregation was observed around the printed scaffold, indicating that the PLA scaffold and the composite scaffold had good biocompatibility and did not cause an inflammatory reaction and tissue necrosis. HE images showed the growth of new bone marked by the red arrow. At 1–3 months after surgery, the amount of new bone tissue in the PLA scaffold group and the composite material group increased gradually, indicating that the pore connectivity of the printed scaffold was suitable and new bone tissue could grow through the pore of the scaffold. The new bone in the PLA group was sporadically distributed and increased gradually with time, but the increase rate was slower than that of the composite material group. In the first month of the composite material group, the new bone tissue was closely distributed to the material. Over the next 2 months, the new bone in the composite group's outer layer gradually closed and thickened (Figure 8). 3D CT reconstruction images intuitively demonstrated the osteogenic ability of different materials *in vivo*. The defect in the surgical area of the PLA group was apparent, but the defect in the composite group was not visible in the appearance at the third month after surgery (Figure 9a). Then, a cortical region with a diameter of 0.5 cm of the implanted scaffold was separately 3D reconstructed. The reconstructed images showed that the results were consistent with the HE. The PLA group was porous with obvious surface vacancy. Meanwhile, the new bone in the outer layer showed compactness from the second month postoperatively in the composite group (Figure 9b). The quantized density of the material area (MD) and the volume of bone growth (BV/TV) also proved that the osteogenic ability of the composite group was better than that of the PLA group *in vivo* (Figures 9c and d and 10).

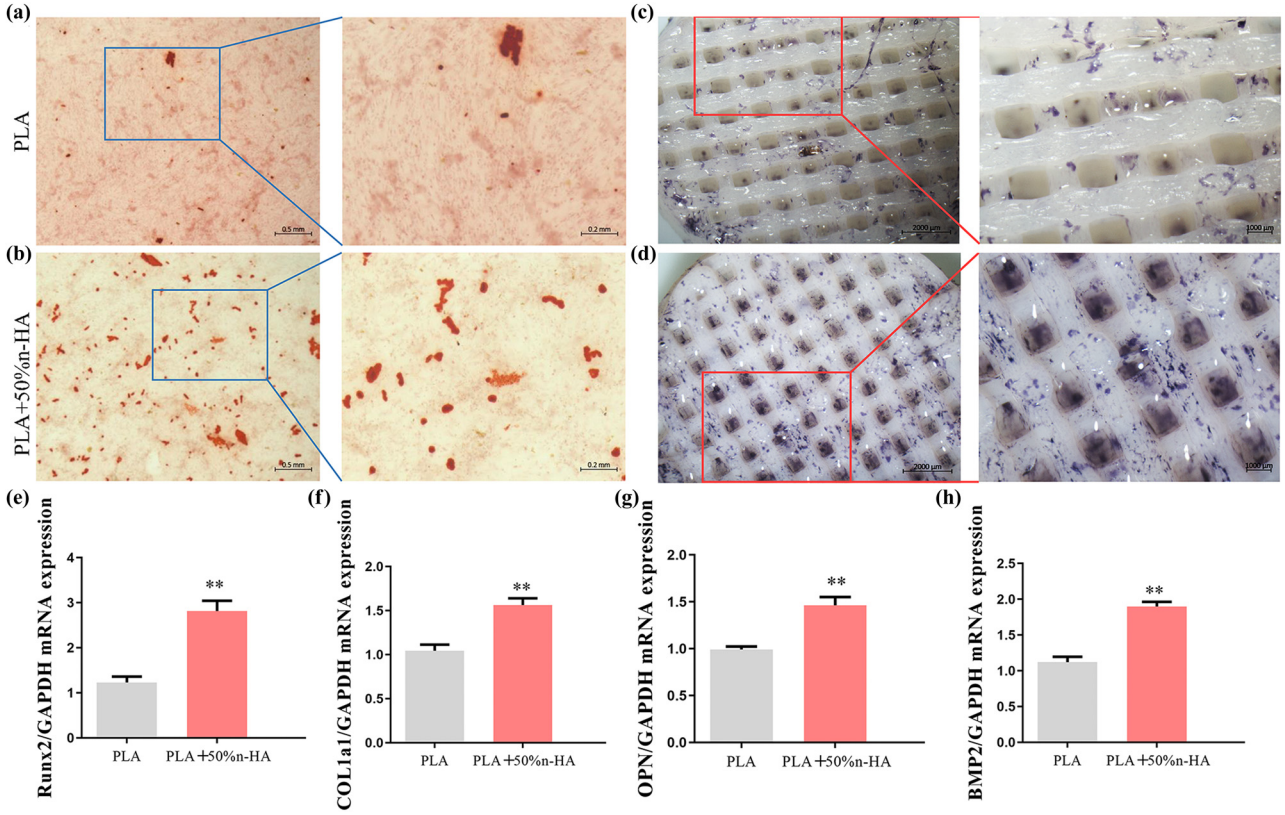

Figure 7: Osteogenic induction of 3D-printed scaffolds. (a) Mineralized extracellular matrix production of BMSCs on PLA scaffolds; (b) alizarin red S staining of BMSCs on PLA/n-HA composites scaffolds; (c) alkaline phosphatase activity of BMSCs was conducted on PLA scaffolds; (d) results of induction effect of BMSCs of alkaline phosphatase staining on PLA/n-HA composites scaffolds (bar, low power = 0.5 mm; high power = 0.2 mm); and (e–h) the expression of osteogenic genes in BMSCs on PLA and PLA/n-HA composites scaffolds. Runt-related transcription factor 2 (*Runx2*), type I collagen a1 (*Col1a1*), osteopontin (*OPN*), and bone morphogenetic protein-2 (*BMP2*), $^{**}p < 0.05$.

4 Discussion

As a temporary scaffold, the implant provides a suitable environment for cell adhesion and growth and has the ability of bone conduction and osteoinduction to guide bone regeneration and growth [8,33]. The materials and the structure of the scaffold affect the mechanical properties, biological reactions, oxygen, nutrients, and waste transport of the entire scaffold [34]. Although a wide variety of materials have been used in the design of tissue-engineered scaffolds, including metals [35] and ceramics [36]. Polymer materials are the most common, largely because they are easy to manufacture, their structural chemistry and mechanical properties are very similar to the natural extracellular matrix of many tissue types [37,38]. Polymers provide adequate mechanical support, but lack osteogenic induction [16,18]. $Ca_{10}(PO_4)_6(OH)_2$ with a calcium to phosphorus ratio of 1.67 is also known as HA. HA is the main inorganic part of human bones and teeth and is widely used as the raw material for bone and tooth filling [33,39]. Although the mechanical strength of sintered ceramic scaffolds is usually only 0.17–0.64 MPa, which cannot bear the load, they have good cell activity [7]. HA is suggested to be used as bone fillers rather than scaffolds for the fabrication of load-bearing bone repair scaffolds [31,32]. In this study, the composites were first prepared, and the composition was analyzed. The absence of chlorine in the composites proved that the organic solution had been completely removed during the processing. The composite was printable and could be printed out of various shapes, including squares and cylinders, according to the printing blueprint. To clearly present the precision of printing, CT scan and 3D reconstruction were carried out on the printed samples, and the laminated structure of the inner layer, which naked eyes could not see, could also be observed. Then, the microstructure of the composite was further observed. According to the SEM results, both the cross section of the filament and the surface of the scaffold, the composite scaffold with n-HA was significantly rougher than the

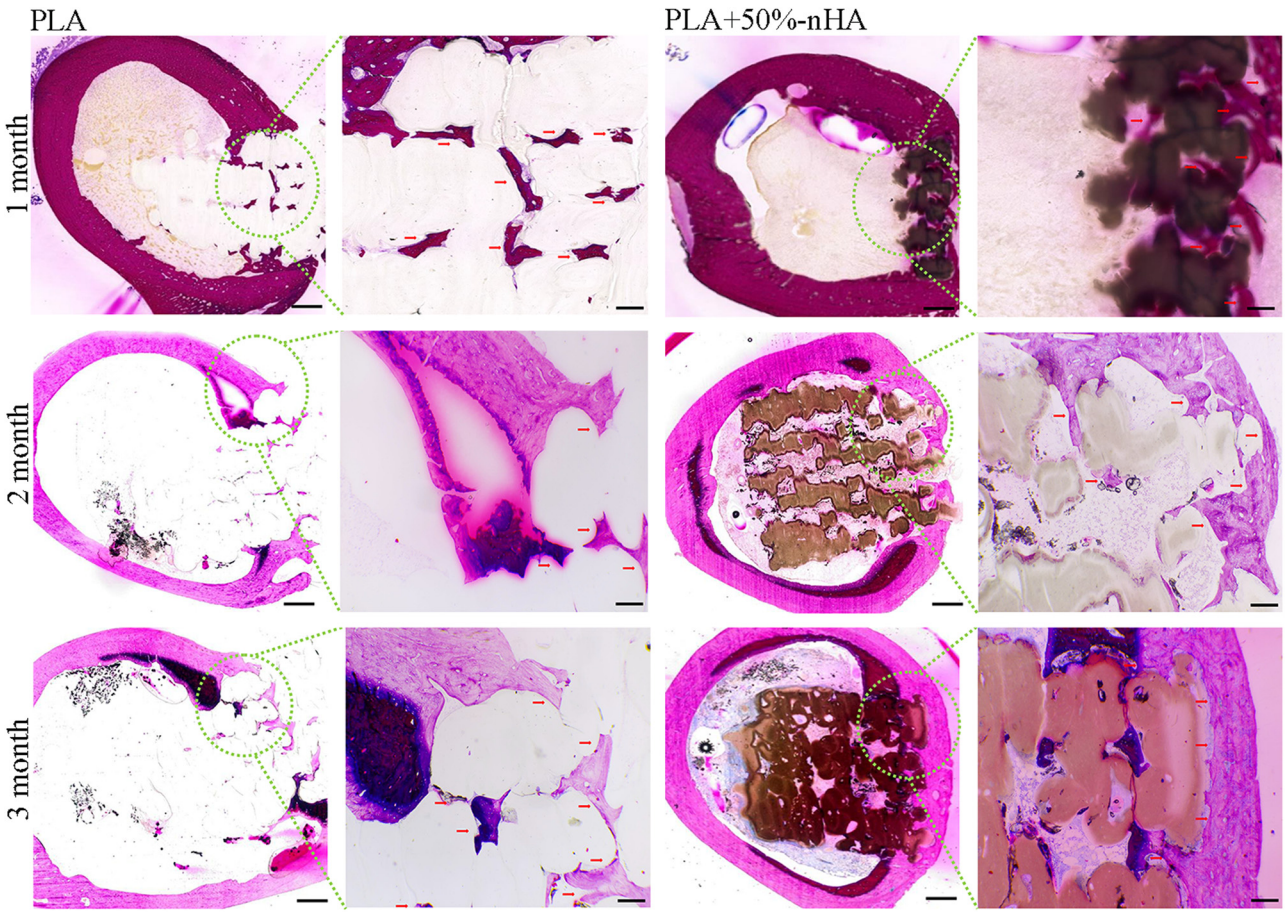

Figure 8: Hematoxylin–eosin (HE) staining of the implanted scaffolds. New bone growth of PLA and PLA/n-HA composite scaffolds were observed at 1, 2, and 3 months after implantation. The observation of the whole interface are shown in the first and third columns.

PLA scaffold. The rough surface increased the surface area of the scaffold, and the space for cell growth was enlarged accordingly.

Natural bone contains an equal proportion of organic phase and inorganic phase (calcium phosphates) [11]. We tried to simulate collagen with PLA, mixed with 50% n-HA, corresponding to the organic and inorganic phases in natural bone. Our previous study proved that the proportion of 50% n-HA was also the highest proportion that could be used for FDM printing. When the n-HA is higher than 50%, the filament is too brittle to pass through the FDM printing nozzle continuously [40]. Then, the mechanical test was carried out on the printed scaffold, and the results showed that the material's mechanical properties decreased after adding n-HA. The decrease of mechanical properties was related to the brittleness of Ca-P and the ductility of PLA. The addition of a large number of HA particles significantly changed the morphology of PLA and damaged the continuity. Although some studies have reported that the addition of HA leads to a mechanical improvement, the amount of HA added in those studies was small (less than 15%), which was far lower than the 50% used in this study [41]. We did not pursue the strongest mechanical properties because even if the mechanics were reduced, the mechanical effects of the composites were still sufficient. The ultimate stress of the scaffold after the addition of n-HA was still 17.8 MPa, which is higher than that of the natural human cancellous bone (1–12 MPa) [42]. In addition, n-HA can significantly increase the osteoinductivity of the scaffold [9] and neutralize the acidity of the lactic acid produced after PLA degradation [43,44].

The selection and shaping of the pore structure is a critical step in the fabrication of 3D scaffolds. In the structure of the natural bone, cortical bone, which is the dense outer layer of the bone, has a porosity of less than 10%. Meanwhile, the cancellous bone is spongy and has a porosity of 50–90% [11]. The pore structure affects

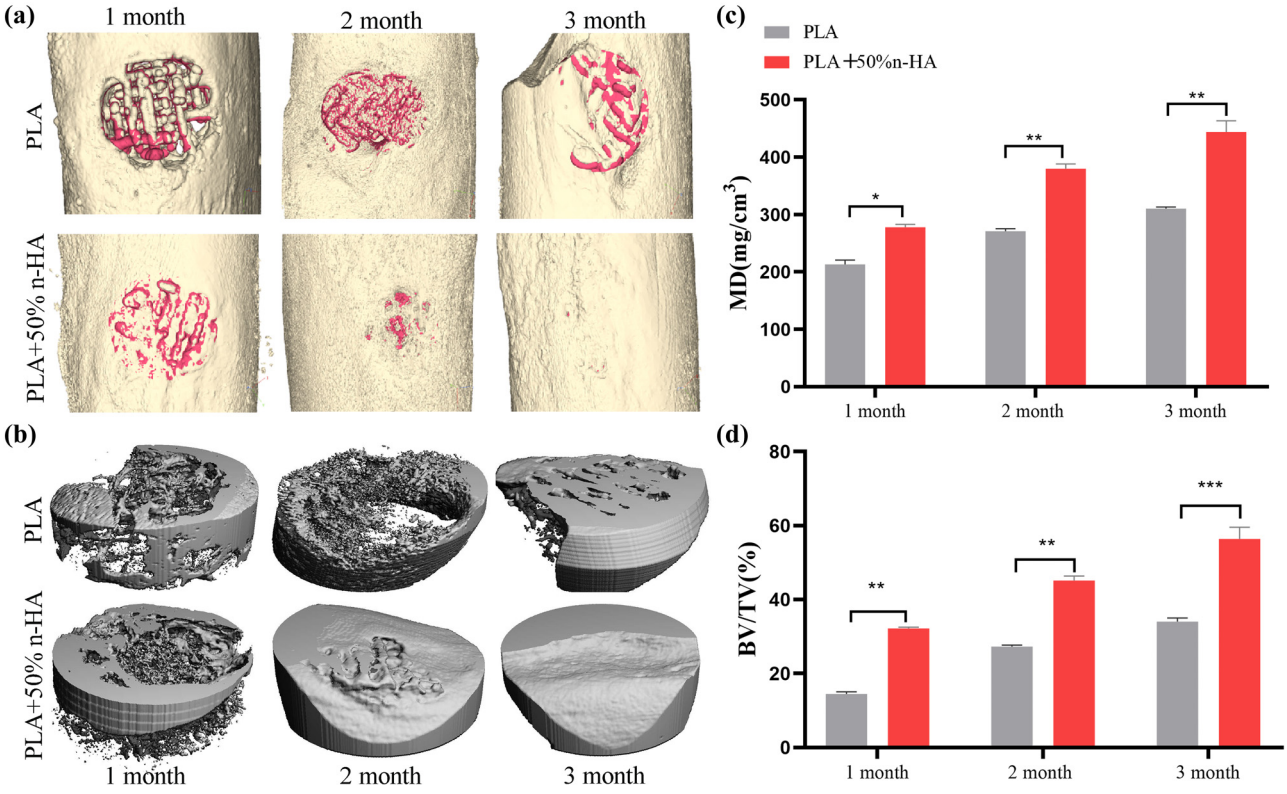

Figure 9: Micro-CT analysis of the implanted scaffolds. The PLA and PLA/n-HA composite scaffolds were implanted into the defect of the rabbit femoral. (a) At 1, 2, and 3 months after scaffold implantation, the bone defect area was scanned using micro-CT, and 3D reconstruction was performed. The reconstructed scaffold was shown in red and the bone in gold; (b) the scaffold-implanted area of the cortical bone (5 mm in diameter and 2 mm in depth) was reconstructed in 3D; and (c and d) quantitative calculation of new bone growth based on CT data, mineral density (MD), and bone tissue volume (BV)/total tissue volume/(TV). *$p < 0.05$; **$p < 0.01$, ***$p < 0.001$.

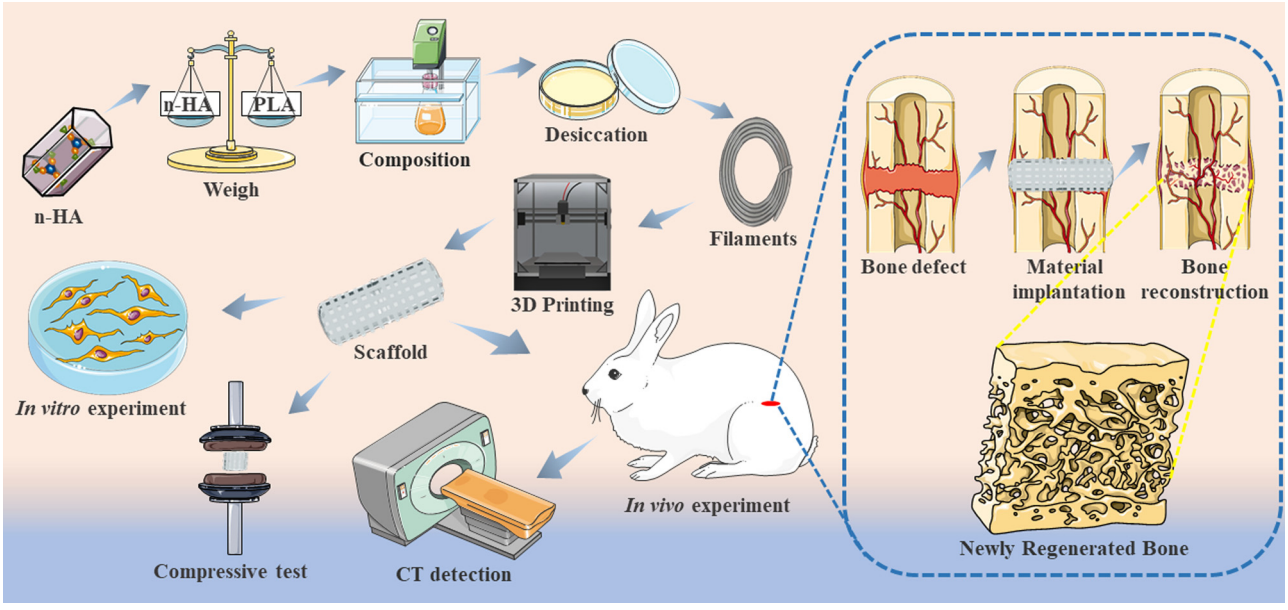

Figure 10: Schematic illustration of the experimental process. PLA and n-HA were uniformly mixed in a 50:50% ratio to make the composite material. Composite scaffolds were printed for material characterization and *in vitro* and *in vivo* experiments.

mechanical properties. The compressive strength and Young's modulus of the cortical bone are significantly stronger than that of the cancellous bone [45]. The pore structure is also the continuous inward growth and material exchange channels of bone tissue. Liquid can be nourished and transported through the pores. Migrated stem cells, bone cells, macrophages, and other cells can cross grow through the pores [7,45]. The artificial porous scaffolds used to repair bone defects can promote nutrient transport, new bone growth, and blood vessel growth when the macropore size of the scaffolds is 100–500 μm [46,47]. It can be clearly seen from the SEM images that the macropore size of the scaffold manufactured in this study was between 300 and 400 μm, which met the requirements. *In vitro* experiments were used to demonstrate the biocompatibility and osteogenic inducibility of the scaffolds. BMSCs could attach, grow, proliferate, and extend pseudopods on the printed scaffold. The markers of each stage of osteogenesis were also detected. In the composite scaffold group, *Runx2* of osteoprogenitor [48], *COL1a1* and *ALP* of pre-osteoblast and mature osteoblast [49], and *OPN* of osteocyte were significantly overexpressed of the PLA scaffold group [50]. It proved that BMSCs were all promoted by composite in the osteogenic lineage commitment, matrix maturation, mineralization, and terminal differentiation stages. Finally, in the *in vivo* experiment, the new bone growth of the composite material group was significantly higher than that of the PLA group. The new bone data of the PLA group at the third month after surgery could be similar to that of the composite material group at the first month after surgery. However, PLA/n-HA composite scaffolds have some disadvantages, such as the active ingredients of the raw materials may be destroyed due to the heating process during FDM printing. It is difficult to modify raw materials by directly adding growth factors and proteins [13,51,52]. In the future, we will carry out the secondary processing of the printed scaffold, including the bioactive coating on the surface.

In conclusion, the composite material with high n-HA content was manufactured, and the composite scaffold was printed by the FDM 3D printing technology in this study. The composite scaffold has printability, biocompatibility, and osteogenic induction and can induce new bone growth *in vivo*. The PLA/n-HA composite scaffold has a high potential for use as implants for the critical bone defect. Composite materials can combine the advantages and make up for the shortcomings of each material. The development of composite materials has a guiding significance for the application of personalized biomaterials.

Funding information: This work was partially supported by the National Key Research and Development Program of China (2018YFC1106800). National Natural Science Foundation of China (31971251 and 81874002). Sichuan Province Science & Technology Department Projects (2016CZYD0004, 2019JDTD0008, 2019YFH0079, 2017SZ0195, 2019JDRC0100, and 2020JDRC0054). National Clinical Research Center for Geriatrics, West China Hospital, Sichuan University (Y2018B22 and Z20192013) and West China Hospital Postdoctoral Research and Development Fund (2019HXBH068).

Author contributions: All authors have accepted responsibility for the entire content of this manuscript and approved its submission.

Conflict of interest: The authors state no conflict of interest.

References

[1] Ho-Shui-Ling A, Bolander J, Rustom LE, Johnson AW, Luyten FP, Picart C. Bone regeneration strategies: engineered scaffolds, bioactive molecules and stem cells current stage and future perspectives. Biomaterials. 2018;180:143–62.

[2] Pape HC, Evans A, Kobbe P. Autologous bone graft: properties and techniques. J Orthop Trauma. 2010;24(Suppl 1): S36–40.

[3] Rogers GF, Greene AK. Autogenous bone graft: basic science and clinical implications. J Craniofac Surg. 2012;23(1):323–7.

[4] Cheng L, Suresh KS, He H, Rajput RS, Feng Q, Ramesh S, et al. 3D printing of micro- and nanoscale bone substitutes: a review on technical and translational perspectives. Int J Nanomed. 2021;16:4289–319.

[5] Holzapfel BM, Reichert JC, Schantz JT, Gbureck U, Rackwitz L, Noth U, et al. How smart do biomaterials need to be? A translational science and clinical point of view. Adv Drug Deliv Rev. 2013;65(4):581–603.

[6] Cao S, Zhao Y, Hu Y, Zou L, Chen J. New perspectives: in-situ tissue engineering for bone repair scaffold. Compos Part B Eng. 2020;202:108445.

[7] Wang C, Huang W, Zhou Y, He L, He Z, Chen Z, et al. 3D printing of bone tissue engineering scaffolds. Bioact Mater. 2020;5(1):82–91.

[8] Goncalves AM, Moreira A, Weber A, Williams GR, Costa PF. Osteochondral tissue engineering: the potential of electrospinning and additive manufacturing. Pharmaceutics. 2021;13:7.

[9] Askari M, Afzali Naniz M, Kouhi M, Saberi A, Zolfagharian A, Bodaghi M. Recent progress in extrusion 3D bioprinting of hydrogel biomaterials for tissue regeneration: a comprehensive review with focus on advanced fabrication techniques. Biomater Sci. 2021;9(3):535–73.

[10] Zhu G, Zhang T, Chen M, Yao K, Huang X, Zhang B, et al. Bone physiological microenvironment and healing mechanism: Basis for future bone-tissue engineering scaffolds. Bioact Mater. 2021;6(11):4110–40.
[11] Garot C, Bettega G, Picart C. Additive manufacturing of material scaffolds for bone regeneration: toward application in the clinics. Adv Funct Mater. 2020;31(5):2006967.
[12] Kim HD, Amirthalingam S, Kim SL, Lee SS, Rangasamy J, Hwang NS. Biomimetic materials and fabrication approaches for bone tissue engineering. Adv Healthc Mater. 2017;6:23.
[13] Kang SW, Bae JH, Park SA, Kim WD, Park MS, Ko YJ, et al. Combination therapy with BMP-2 and BMSCs enhances bone healing efficacy of PCL scaffold fabricated using the 3D plotting system in a large segmental defect model. Biotechnol Lett. 2012;34(7):1375–84.
[14] Sa MW, Nguyen BB, Moriarty RA, Kamalitdinov T, Fisher JP, Kim JY. Fabrication and evaluation of 3D printed BCP scaffolds reinforced with ZrO2 for bone tissue applications. Biotechnol Bioeng. 2018;115(4):989–99.
[15] Haleem A, Javaid M. Role of CT and MRI in the design and development of orthopaedic model using additive manufacturing. J Clin Orthop Trauma. 2018;9(3):213–7.
[16] Mazzanti V, Malagutti L, Mollica F. FDM 3D printing of polymers containing natural fillers: a review of their mechanical properties. Polym (Basel). 2019;11:7.
[17] Ngo TD, Kashani A, Imbalzano G, Nguyen KTQ, Hui D. Additive manufacturing (3D printing): a review of materials, methods, applications and challenges. Compos Part B Eng. 2018;143:172–96.
[18] Jakus AE, Rutz AL, Jordan SW, Kannan A, Mitchell SM, Yun C, et al. Hyperelastic "bone": a highly versatile, growth factor-free, osteoregenerative, scalable, and surgically friendly biomaterial. Sci Transl Med. 2016;8(358):358ra127.
[19] Diomede F, D'Aurora M, Gugliandolo A, Merciaro I, Orsini T, Gatta V, et al. Biofunctionalized scaffold in bone tissue repair. Int J Mol Sci. 2018;19:4.
[20] Pizzicannella J, Diomede F, Gugliandolo A, Chiricosta L, Bramanti P, Merciaro I, et al. 3D printing PLA/gingival stem cells/EVs upregulate miR-2861 and -210 during osteoangiogenesis commitment. Int J Mol Sci. 2019;20:13.
[21] Wang W, Zhang B, Li M, Li J, Zhang C, Han Y, et al. 3D printing of PLA/n-HA composite scaffolds with customized mechanical properties and biological functions for bone tissue engineering. Compos Part B Eng. 2021;224:109192.
[22] Lin S, Dong P, Zhou C, Dallan LAP, Zimin VN, Pereira GTR, et al. Degradation modeling of poly-l-lactide acid (PLLA) bioresorbable vascular scaffold within a coronary artery. Nanotechnol Rev. 2020;9(1):1217–26.
[23] Gugliandolo A, Diomede F, Cardelli P, Bramanti A, Scionti D, Bramanti P, et al. Transcriptomic analysis of gingival mesenchymal stem cells cultured on 3D bioprinted scaffold: a promising strategy for neuroregeneration. J Biomed Mater Res Part A. 2018;106(1):126–37.
[24] Haleem A, Javaid M, Khan RH, Suman R. 3D printing applications in bone tissue engineering. J Clin Orthop Trauma. 2020;11(Suppl 1):S118–24.
[25] Wu Q, Xu S, Wang X, Jia B, Han Y, Zhuang Y, et al. Complementary and synergistic effects on osteogenic and angiogenic properties of copper-incorporated silicocarnotite bioceramic: in vitro and in vivo studies. Biomaterials. 2021;268:120553.
[26] Wang Y, Cao X, Ma M, Lu W, Zhang B, Guo Y. A GelMA-PEGDA-nHA composite hydrogel for bone tissue engineering. Mater (Basel). 2020;13:17.
[27] Alinda Shaly A, Hannah Priya G, Mary Linet J. An exploration on the configurational and mechanical aspects of hydrothermally procured MgO/HA bioceramic nanocomposite. Phys B Condens Matter. 2021;617:413131.
[28] Manohar CS, Kumar BS, Sadhu SPP, Srimadh SK, Muthukumar VS, Venketesh S, et al. Novel lead-free biocompatible piezoelectric hydroxyapatite (HA) – BCZT ($Ba_{0.85}Ca_{0.15}Zr_{0.1}Ti_{0.9}O_3$) nanocrystal composites for bone regeneration. Nanotechnol Rev. 2019;8(1):61–78.
[29] Zou Z, Wang L, Zhou Z, Sun Q, Liu D, Chen Y, et al. Simultaneous incorporation of PTH(1-34) and nano-hydroxyapatite into chitosan/alginate hydrogels for efficient bone regeneration. Bioact Mater. 2021;6(6):1839–51.
[30] Jian W, Hui D, Lau D. Nanoengineering in biomedicine: current development and future perspectives. Nanotechnol Rev. 2020;9(1):700–15.
[31] Yang X, Li Y, Liu X, Zhang R, Feng Q. In vitro uptake of hydroxyapatite nanoparticles and their effect on osteogenic differentiation of human mesenchymal stem cells. Stem Cell Int. 2018;2018:2036176.
[32] Shi X, Zhou K, Huang F, Zhang J, Wang C. Endocytic mechanisms and osteoinductive profile of hydroxyapatite nanoparticles in human umbilical cord Wharton's jelly-derived mesenchymal stem cells. Int J Nanomed. 2018;13:1457–70.
[33] Kupikowska-Stobba B, Kasprzak M. Fabrication of nanoparticles for bone regeneration: new insight into applications of nanoemulsion technology. J Mater Chem B. 2021;9(26):5221–44.
[34] Ahn G, Park JH, Kang T, Lee JW, Kang HW, Cho DW. Effect of pore architecture on oxygen diffusion in 3D scaffolds for tissue engineering. J Biomech Eng. 2010;132(10):104506.
[35] Pei X, Wu L, Lei H, Zhou C, Fan H, Li Z, et al. Fabrication of customized Ti6Al4V heterogeneous scaffolds with selective laser melting: optimization of the architecture for orthopedic implant applications. Acta Biomater. 2021;126:485–95.
[36] Zhang B, Sun H, Wu L, Ma L, Xing F, Kong Q, et al. 3D printing of calcium phosphate bioceramic with tailored biodegradation rate for skull bone tissue reconstruction. Bio-Design Manuf. 2019;2(3):161–71.
[37] Tibbitt MW, Anseth KS. Hydrogels as extracellular matrix mimics for 3D cell culture. Biotechnol Bioeng. 2009;103(4):655–63.
[38] Liang X, Gao J, Xu W, Wang X, Shen Y, Tang J, et al. Structural mechanics of 3D-printed poly(lactic acid) scaffolds with tetragonal, hexagonal and wheel-like designs. Biofabrication. 2019;11(3):035009.
[39] Boller LA, Shiels SM, Florian DC, Peck SH, Schoenecker JG, Duvall C, et al. Effects of nanocrystalline hydroxyapatite concentration and skeletal site on bone and cartilage formation in rats. Acta Biomater. 2021;130:485–96.
[40] Zhang B, Wang L, Song P, Pei X, Sun H, Wu L, et al. 3D printed bone tissue regenerative PLA/HA scaffolds with comprehensive performance optimizations. Mater Des. 2021;201:109490.
[41] Milazzo M, Contessi Negrini N, Scialla S, Marelli B, Farè S, Danti S, et al. Additive manufacturing approaches for

hydroxyapatite-reinforced composites. Adv Funct Mater. 2019;29:35.
[42] Zhang B, Pei X, Song P, Sun H, Li H, Fan Y, et al. Porous bioceramics produced by inkjet 3D printing: effect of printing ink formulation on the ceramic macro and micro porous architectures control. Compos Part B Eng. 2018;155:112–21.
[43] Jaidev LR, Chatterjee K. Surface functionalization of 3D printed polymer scaffolds to augment stem cell response. Mater Des. 2019;161:44–54.
[44] Chen X, Gao C, Jiang J, Wu Y, Zhu P, Chen G. 3D printed porous PLA/nHA composite scaffolds with enhanced osteogenesis and osteoconductivity in vivo for bone regeneration. Biomed Mater. 2019;14(6):065003.
[45] Zhang B, Pei X, Zhou C, Fan Y, Jiang Q, Ronca A, et al. The biomimetic design and 3D printing of customized mechanical properties porous Ti6Al4V scaffold for load-bearing bone reconstruction. Mater Des. 2018;152:30–9.
[46] Xu Y, Xu GY, Tang C, Wei B, Pei X, Gui JC, et al. Preparation and characterization of bone marrow mesenchymal stem cell-derived extracellular matrix scaffolds. J Biomed Mater Res B Appl Biomater. 2015;103(3):670–8.
[47] Huang J, Liu W, Liang Y, Li L, Duan L, Chen J, et al. Preparation and biocompatibility of diphasic magnetic nanocomposite scaffold. Mater Sci Eng C Mater Biol Appl. 2018;87:70–7.
[48] Qin X, Jiang Q, Komori H, Sakane C, Fukuyama R, Matsuo Y, et al. Runt-related transcription factor-2 (Runx2) is required for bone matrix protein gene expression in committed osteoblasts in mice. J Bone Min Res. 2021. doi: 10.1002/jbmr.4386.
[49] Li X, Zhang B, Wang H, Zhao X, Zhang Z, Ding G, et al. The effect of aging on the biological and immunological characteristics of periodontal ligament stem cells. Stem Cell Res Ther. 2020;11(1):326.
[50] Peng S, Shi S, Tao G, Li Y, Xiao D, Wang L, et al. JKAMP inhibits the osteogenic capacity of adipose-derived stem cells in diabetic osteoporosis by modulating the Wnt signaling pathway through intragenic DNA methylation. Stem Cell Res Ther. 2021;12(1):120.
[51] Wang L, Xu W, Chen Y, Wang J. Alveolar bone repair of rhesus monkeys by using BMP-2 gene and mesenchymal stem cells loaded three-dimensional printed bioglass scaffold. Sci Rep. 2019;9(1):18175.
[52] Santo VE, Gomes ME, Mano JF, Reis RL. Controlled release strategies for bone, cartilage, and osteochondral engineering – Part II: challenges on the evolution from single to multiple bioactive factor delivery. Tissue Eng Part B Rev. 2013;19(4):327–52.